Systematic analysis of Ca²⁺ homeostasis in *Saccharomyces cerevisiae* based on chemical-genetic interaction profiles

Farzan Ghanegolmohammadi[a,†], Mitsunori Yoshida[a,†], Shinsuke Ohnuki[a], Yuko Sukegawa[a,b], Hiroki Okada[a,c], Keisuke Obara[d], Akio Kihara[d], Kuninori Suzuki[a,e], Tetsuya Kojima[a], Nozomu Yachie[f,g], Dai Hirata[h,i], and Yoshikazu Ohya[a,*]

[a]Department of Integrated Biosciences and [e]Bioimaging Center, Graduate School of Frontier Sciences, University of Tokyo, Kashiwa 277-8562, Japan; [b]AIST-UTokyo Advanced Operand-Measurement Technology Open Innovation Laboratory, Kashiwa 277-0882, Japan; [c]Department of Cell and Developmental Biology, Perelman School of Medicine, University of Pennsylvania, Philadelphia, PA 19104-6058; [d]Faculty of Pharmaceutical Sciences, Hokkaido University, Sapporo 060-0812, Japan; [f]Synthetic Biology Division, Research Center for Advanced Science and Technology, University of Tokyo, Tokyo 153-8904, Japan; [g]PRESTO, Japan Science and Technology Agency, Tokyo 102-0076, Japan; [h]Research and Development Department, Asahi Sake Brewing Co., Nagaoka 949-5494, Japan; [i]Department of Molecular Biotechnology, Graduate School of Advanced Sciences of Matter, Hiroshima University, Higashi-Hiroshima 739-8530, Japan

ABSTRACT We investigated the global landscape of Ca²⁺ homeostasis in budding yeast based on high-dimensional chemical-genetic interaction profiles. The morphological responses of 62 Ca²⁺-sensitive (*cls*) mutants were quantitatively analyzed with the image processing program CalMorph after exposure to a high concentration of Ca²⁺. After a generalized linear model was applied, an analysis of covariance model was used to detect significant Ca²⁺–*cls* interactions. We found that high-dimensional, morphological Ca²⁺–*cls* interactions were mixed with positive (86%) and negative (14%) chemical-genetic interactions, whereas one-dimensional fitness Ca²⁺–*cls* interactions were all negative in principle. Clustering analysis with the interaction profiles revealed nine distinct gene groups, six of which were functionally associated. In addition, characterization of Ca²⁺–*cls* interactions revealed that morphology-based negative interactions are unique signatures of sensitized cellular processes and pathways. Principal component analysis was used to discriminate between suppression and enhancement of the Ca²⁺-sensitive phenotypes triggered by inactivation of calcineurin, a Ca²⁺-dependent phosphatase. Finally, similarity of the interaction profiles was used to reveal a connected network among the Ca²⁺ homeostasis units acting in different cellular compartments. Our analyses of high-dimensional chemical-genetic interaction profiles provide novel insights into the intracellular network of yeast Ca²⁺ homeostasis.

INTRODUCTION

Calcium is an essential component of eukaryotic cells. Although present in low concentration, intracellular Ca²⁺ is important for structural, enzymatic, and signaling roles in many cellular pathways (Williams, 1999). High levels of cytosolic Ca²⁺ are considered damaging because of precipitation with organic anions. For this reason, eukaryotic cells have a variety of homeostatic mechanisms to

effectively acquire, use, and store Ca^{2+} and keep intracellular levels of Ca^{2+} at a nontoxic level (Cyert and Philpott, 2013).

The budding yeast *Saccharomyces cerevisiae* has been used as a eukaryotic model organism to study Ca^{2+} homeostasis. In *S. cerevisiae*, the concentration of free cytosolic Ca^{2+} is maintained between 50 and 200 nM, whereas its concentration in the environment ranges from <1 µM to >100 mM (Halachmi and Eilam, 1993; Cui and Kaandorp, 2006; Cui *et al.*, 2009). A key element in Ca^{2+} homeostasis is its intracellular compartmentalization. Ca^{2+} pools are classified as exchangeable or nonexchangeable based on pulse-chase experiments (Eilam, 1981). Most of the nonexchangeable pools reside in cellular compartments, such as the vacuole and the endoplasmic reticulum (ER), and the exchangeable pools are believed to be located in the cytosol (Eilam, 1981; Eilam *et al.*, 1985; Tanida *et al.*, 1996).

The vacuole is the primary Ca^{2+}-storage organelle in yeast, containing >90% of the intracellular Ca^{2+} (Dunn *et al.*, 1994). A vacuolar Ca^{2+}-transporting ATPase, Pmc1p, plays an important role in the sequestration of cytosolic Ca^{2+} into the vacuole, and *pmc1* mutants exhibit reduced vacuolar Ca^{2+} content, resulting in a Ca^{2+}-sensitivity growth phenotype (Cunningham and Fink, 1994). This *pmc1* mutant phenotype is aggravated by disruption of the vacuolar H^+-Ca^{2+} exchanger Vcx1p because Pmc1p and Vcx1p coordinate to maintain cytosolic Ca^{2+} homeostasis. Calmodulin, a major intracellular Ca^{2+}-binding protein, is ubiquitous in eukaryotic cells, and the Ca^{2+}/calmodulin signaling pathway responds to elevated cytosolic Ca^{2+}. In response to the increased signal, Ca^{2+}/calmodulin binds to calcineurin, the Ca^{2+}/calmodulin-dependent phosphatase. Calcineurin up-regulates transcription of *PMC1* via activation of the transcription factor Crz1p and negatively regulates Vcx1p by an unknown mechanism (Cunningham and Fink, 1996; Stathopoulos and Cyert, 1997; Pittman *et al.*, 2004). Vacuolar proton-translocating ATPase (V-ATPase) *VMA* genes are also important for Ca^{2+} homeostasis (Ohya *et al.*, 1991; Umemoto *et al.*, 1991; Bachhawat *et al.*, 1993; Hirata *et al.*, 1993; Ho *et al.*, 1993). Studies have shown that the proton-motive force driven by V-ATPase is required for activation of Ca^{2+} transporters in the vacuole, including Vcx1p (Cunningham and Fink, 1996; Pozos *et al.*, 1996; Förster and Kane, 2000). The vacuole also has a counteracting Ca^{2+} release channel, Yvc1p, which depends on elevated cytosolic Ca^{2+} levels for its activity (Chang *et al.*, 2010). Overexpression of Yvc1p results in elevation of cytosolic Ca^{2+} and Ca^{2+} sensitivity (Denis and Cyert, 2002).

In addition to the vacuole, the ER and the plasma membrane are also involved in Ca^{2+} homeostasis. The Ca^{2+} concentration in the lumen of the ER is much higher than in the cytosol (Demaurex and Frieden, 2003) and the ER contains several Ca^{2+}-dependent enzymes. Calcium-sensitive 2p (Cls2p)/Csg2p encodes a regulatory subunit of mannosylinositol phosphorylceramide (MIPC) synthase, which is involved in sphingolipid metabolism and the regulation of Ca^{2+} homeostasis in the ER lumen (Beeler *et al.*, 1994; Takita *et al.*, 1995; Tanida *et al.*, 1996). The plasma membrane has an additional mechanism for the regulation of Ca^{2+} influx called a high-affinity Ca^{2+} influx system (HACS), which is composed of at least three components, including Cch1p, Ecm7p, and Mid1p (Cunningham, 2011). Maintaining Ca^{2+} homeostasis through the HACS is necessary for adaptation and survival of the cells during mating processes (Iida *et al.*, 1994; Fischer *et al.*, 1997; Martin *et al.*, 2011).

A genetic interaction refers to a phenotype caused by combining the effects of individual genetic variants. In general, based on the differences between observed and expected double-mutant phenotypes, genetic interactions can be classified into two groups,

those with positive or negative interactions (Dixon *et al.*, 2009). A negative genetic interaction describes a double mutant in which the phenotype is stronger than expected. The most extreme case of a negative fitness interaction is synthetic lethality, in which the combination of two mutations results in an inviable phenotype (Mani *et al.*, 2008; Baryshnikova *et al.*, 2013). Similar to genetic interactions, a chemical-genetic interaction refers to a phenotype caused by combining the effects of chemicals and genetic variants. Chemical synthetic lethality is a negative interaction in which a chemical compound causes lethality in a particular mutant. On the other hand, a positive genetic interaction indicates a double mutant with less defective fitness than expected (Mani *et al.*, 2008; Baryshnikova *et al.*, 2013). Along the same line, a positive chemical-genetic interaction is a suppression or masking of effects of a chemical compound in a particular mutant.

Genetic analysis of Ca^{2+}-sensitive (*cls*) mutants in yeast uncovered a variety of genes required for Ca^{2+} homeostasis and Ca^{2+} tolerance. Genome-wide screening of the *cls* mutants unable to grow in the presence of 100 mM $CaCl_2$ (Ohya *et al.*, 1986b; Sambade *et al.*, 2005; Ohnuki *et al.*, 2007; Zhao *et al.*, 2013) has led to the comprehensive identification of components directly or indirectly involved in intracellular Ca^{2+} homeostasis. More than 60 *cls* mutants defective in Ca^{2+} homeostasis have been isolated, such as *pmc1*, *vma*, and *cls2* mutants (Ohya *et al.*, 1986b; Ohnuki *et al.*, 2007). Note that *cls* mutants exhibit various growth phenotypes, including divalent cation and pH sensitivity and carbon source utilization. *pmc1* mutants exhibit a Ca^{2+}-specific sensitive phenotype, whereas *vma* mutants exhibit broad sensitivity to Ca^{2+}, Mn^{2+}, and Zn^{2+}. Our and other studies have indicated that *cls* mutants exhibit various unique morphological phenotypes in Ca^{2+}-rich conditions (Yu *et al.*, 1996; Ohnuki *et al.*, 2007; Yoshida *et al.*, 2013). These results suggested that the *CLS* genes have diverse cellular functions, including cell morphogenesis, and the entire gene network, involved in Ca^{2+} homeostasis, is not yet fully understood.

The present study investigates the global landscape of Ca^{2+} homeostasis in yeast by analyzing the high-dimensional Ca^{2+}–*cls* interaction profiles of 62 *cls* yeast mutants. To identify Ca^{2+}–*cls* interaction profiles, we quantified the cellular, nuclear, and actin morphology of the 62 *cls* mutants with the image processing system CalMorph (Ohtani *et al.*, 2004; Ohya *et al.*, 2005) in the presence and absence of 100 mM $CaCl_2$. The obtained high-dimensional morphological data were used to define negative and positive interactions between Ca^{2+} and Ca^{2+}-sensitive mutations. In addition, extensive statistical analyses of the interaction profiles revealed functional groups of *CLS* genes, functional correlations between the groups, and a global view of Ca^{2+} homeostasis and the Ca^{2+} regulatory network.

RESULTS

Identification of Ca^{2+}–*cls* interactions using high-dimensional morphological phenotypes

Because high concentrations of Ca^{2+} induce morphological changes in the *cls* mutants, we used morphological characteristics to detect interactions between Ca^{2+} and the *cls* mutations (Ohnuki *et al.*, 2007). Ca^{2+}-induced morphological changes in the *cls* mutants are different from the Ca^{2+}–*cls* interactions, which are a combinatorial effect of Ca^{2+} and the *cls* mutation defined as the differences in the Ca^{2+}-induced morphological changes between wild type and the *cls* mutant, which has been defined in previous genetic interaction studies (Dixon *et al.*, 2009; Jonikas *et al.*, 2009). For each of the 501 morphological parameters, the most appropriate probability distribution model was selected from the Gaussian, gamma, beta, and
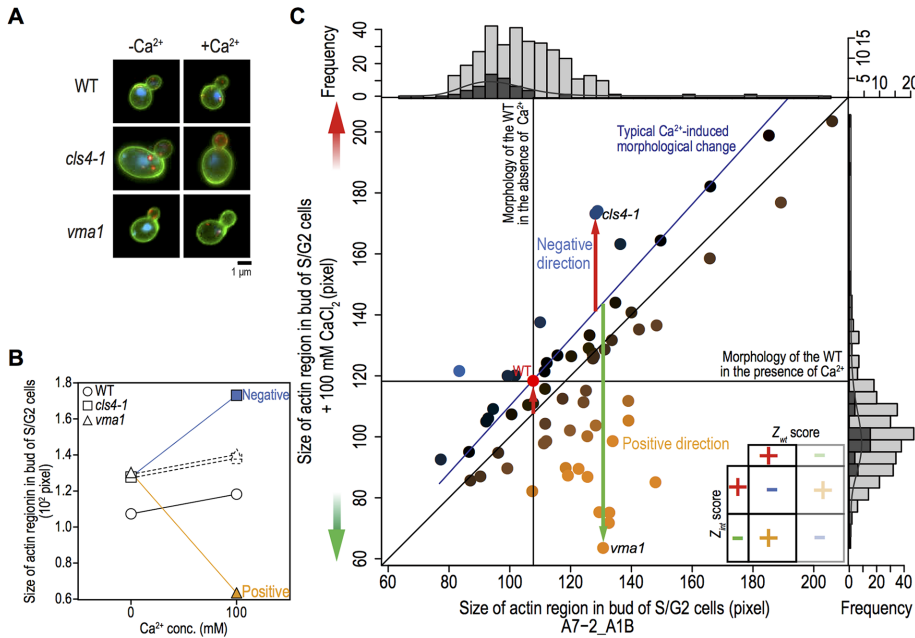
FIGURE 1: Systematic identification of Ca²⁺–*cls* interactions. (A) Representative images during S/G2 phase from five independent experiments. Colors indicate the cell wall (green), actin (red), and DNA (blue). Bar, 1 μm. (B) Size of the actin region in the bud of wild-type S/G2 cells. *cls* mutants in YPD supplemented with or without 100 mM CaCl₂, calculated from the CalMorph parameter value A7-2_A1B, are also shown. Dashed lines indicate the morphological change of each *cls* mutant expected from the morphological change of the wild type. Orange and blue indicate positive and negative Ca²⁺–*cls* interactions, respectively. (C) Parameter values of A7-2_A1B in both wild-type cells and 62 *cls* mutants in the absence (x-axis) or presence (y-axis) of 100 mM CaCl₂. Orange and blue circles indicate positive or negative Ca²⁺–*cls* interactions, respectively, of each *cls* mutant. Vertical and horizontal black lines indicate parameter values of the wild-type cell in the absence or presence, respectively, of 100 mM CaCl₂. The blue line traces typical parameter values expected from the Ca²⁺-induced parameter changes of the wild type. Dark and light gray histograms indicate the distribution of wild type and *cls* mutants in the absence (top) or presence (right) of 100 mM CaCl₂. Gray curve in the histograms represents probability densities of wild-type cells in each condition. Inset, relationships among signs of Z_{wt} scores that indicate the degree of Ca²⁺-induced morphological changes of wild-type cells. Z_{int} scores demonstrate the degree of each Ca²⁺–*cls* interaction and resultant Ca²⁺–*cls* interaction scores (π score; see *Materials and Methods*).

beta-binominal as previously described (Yang *et al.*, 2014), and a generalized linear model was used to standardize the high-dimensional morphological data of wild-type cells and the 62 *cls* mutants. Analysis of covariance (ANCOVA) revealed significant Ca²⁺–*cls* interactions in 209 morphological parameters ($p < 0.05$, likelihood ratio test between two linear models with/without the Ca²⁺–*cls* interaction term), which were summarized into 19 independent morphological features ($p < 0.01$ after the Bonferroni correction; Student's *t* test for correlations between the 19 principal components [PCs] and the 209 parameters; Supplemental Figure S1). These analyses indicated that the Ca²⁺–*cls* interactions of the 62 *cls* mutants were observed in various morphological processes and at different stages of the cell cycle.

Genetic interactions are defined as positive or negative (Dixon *et al.*, 2009). Similarly, interactions between Ca²⁺ and the *cls* mutations were positive or negative (Figure 1). Wild-type yeast cells exhibited an increased actin region in the presence of 100 mM CaCl₂. This region was increased even further in the *cls4-1* mutant (Figure 1, A and B), indicating a negative interaction between Ca²⁺ and *cls4-1*, which can be interpreted as a sensitized Ca²⁺ response caused by the *cls* mutation. In contrast, the size of the actin region in the *vma1* mutant decreased in the presence of 100 mM CaCl₂ (Figure 1, A and

and B), indicating a positive interaction between Ca²⁺ and *vma1*. Opposing directional changes of *cls* mutants were frequently observed in morphological parameters, representing positive interactions. This type of change is characteristic of phenotypic data that change bidirectionally.

The size of the actin region in wild-type cells and the 62 *cls* mutants was mapped in the presence or absence of 100 mM CaCl₂ (Figure 1C), and we defined both positive and negative interaction spaces. When the Ca²⁺-dependent morphological changes of wild-type cells are positive, the regions above and below the expected lines represent negative and positive interactions, respectively (Figure 2A). If the Ca²⁺-dependent morphological changes of wild-type cells are negative, the geometric relationship flips vertically (Figure 2B). Suppression and masking are assigned as positive interactions (Figure 2, A and B), as previously described (Dixon *et al.*, 2009). Standardized variables were calculated as significance from the expected response values of mutant based on corresponding wild-type response, expressed as a π score, and used for further analysis (π > 0 for a positive interaction; π < 0 for a negative interaction).

Feature analysis of the Ca²⁺–*cls* interactions

To understand further the physiological implication of Ca²⁺–*cls* interactions, we performed a feature analysis. First, the majority of the *cls* mutants exhibited more positive interactions than negative interactions (Supplemental Figure S2A). We found that 88.7% (55 of 62) of *cls* mutants exhibited more positive interactions than negative. In other words, 85.73% (1382 of 1612 significant interactions out of 7006 assays, 62 *cls* mutants × 113 parameters, at $p < 0.05$ by Wald test, and false discovery rate [FDR] = 0.24) of the detected interactions were positive. It is notable that all fitness-related Ca²⁺–*cls* interactions were negative because Ca²⁺ has aggravating effects on the growth of Ca²⁺-sensitive mutants. Second, the number of Ca²⁺–*cls* interactions was not correlated with that of Ca²⁺-induced morphological changes in the *cls* mutants (Ohnuki *et al.*, 2007; Supplemental Figure S2B). The number of Ca²⁺–*cls* interactions was less correlated ($R = 0.27$, $p < 0.05$, Student's *t* test) with that of significantly changed parameters in each mutant (Mann–Whitney *U* test, $p < 0.01$), implying that Ca²⁺–*cls* interactions had different implications than with Ca²⁺-induced morphological changes (for complementary information, see Ohnuki *et al.*, 2007). Third, only a small proportion of *cls* mutants exhibited many Ca²⁺–*cls* interactions. Although the number of Ca²⁺–*cls* interactions varied, only 3.22% of the *cls* mutants exhibited >60 Ca²⁺–*cls* interactions (Supplemental Figure S2C). Finally, *cls* mutants with numerous Ca²⁺–*cls* interactions tended to show more severe growth defects in the presence of 100 mM CaCl₂ (Supplemental Figure S2D), suggesting that the *CLS* genes with many Ca²⁺–*cls* interactions may play important roles during cell proliferation and morphogenesis under conditions of high
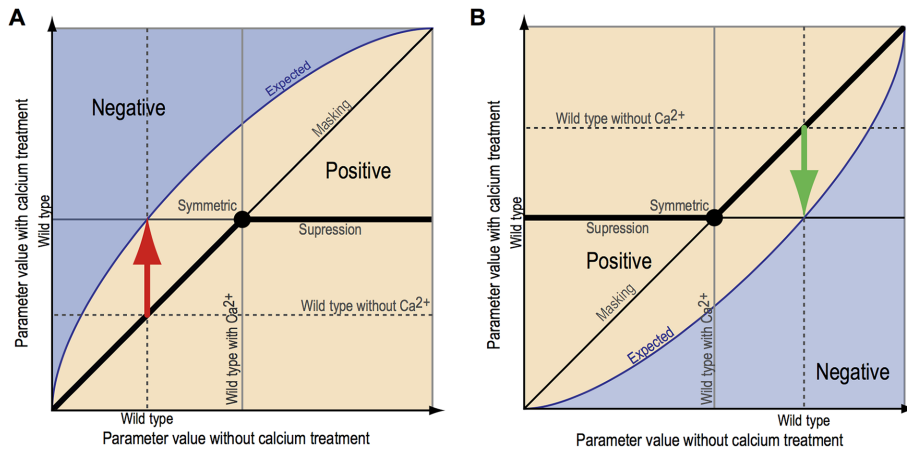
FIGURE 2: Graphical representation of the two types of morphological phenotypes for Ca^{2+}–*cls* interactions. (A, B) Red and green arrows indicate increment and decrement of parameter values of the wild type caused by Ca^{2+} treatment, respectively. Blue lines trace typical parameter values in the presence of high Ca^{2+} expected from the Ca^{2+}-induced morphological changes of wild-type cells. Deviations from the expected value in the same direction with Ca^{2+}-induced morphological changes of the wild type are scored as negative Ca^{2+}-*cls* interactions (depicted in blue). Deviations from the expected values in the opposite direction with Ca^{2+}-induced morphological changes of wild-type cells are classified as positive interactions (depicted in light orange). In positive Ca^{2+}–*cls* interactions, *cls* mutants exhibited fewer Ca^{2+}-induced morphological changes than expected compared with the wild type, which are classified into symmetric, masking, and suppression subcategories, as previously described (Dixon *et al.*, 2009). *cls* mutants also exhibited Ca^{2+}-induced morphological changes in the opposite direction of wild type (lower or higher than the diagonal line in A or B, respectively) and lower or higher level compared with wild type in the presence of 100 mM $CaCl_2$ (lower or higher than the horizontal black line in A or B, respectively).

Ca^{2+}. Thus, the Ca^{2+}–*cls* interaction profiles likely provide a unique source for the understanding of various Ca^{2+} responses in the *cls* mutants.

Clustering analysis of high-dimensional Ca^{2+}–*cls* interaction profiles

To test whether similarities of the Ca^{2+}–*cls* interaction profiles can be used for functional classification of the *CLS* genes, we first extracted the interaction profiles of 16 PCs from 209 parameters by principal component analysis (PCA) and performed clustering analysis with the multiscale bootstrap technique (Suzuki and Shimodaira, 2006; Figure 3). The analysis showed that nine classes, with a total of 49 *cls* mutants (79%), were statistically identified (the approximately unbiased probability value [AU *p*] estimates the probability of observation of a given class in infinite number of classes >0.95; for more information, see Shimodaira, 2002; Figure 3). The defective cellular functions in the mutants of several classes were annotated by gene ontology (Supplemental Table S1). For example, class I consists of 17 V-ATPase–defective mutants (Ohya *et al.*, 1991; Kane, 2006). Class II involves several mutants in the core subunits of homotypic fusion and protein sorting (HOPS) and class C core vacuole/endosome tethering (CORVET) complexes involved in membrane fusion at endosomes, vacuoles, and lysosomes (Balderhaar and Ungermann, 2013). Class IV contains the mutants *cls4-1* and *bem1*, which are defective in Ca^{2+}-modulated bud formation (Yoshida *et al.*, 2013). Class VIII includes *fet3* and *ftr1*, which are defective in iron transport (Kwok *et al.*, 2006). We also noted that the *cls* mutants with related Ca^{2+}–*cls* interaction profiles have similar intracellular Ca^{2+} content. The intracellular Ca^{2+} content in class I, with the exception of *vma22*, was 0.6-fold less than that of wild-type cells, whereas the intracellular Ca^{2+} content of the class II *cls* mutants was

3.1-fold greater than wild type (Supplemental Table S1). Moreover, some *cls* mutants with similar Ca^{2+}–*cls* interaction profiles showed similar divalent cation sensitivity; 29 mutants showed Ca^{2+}-specific sensitivity, such as mutants of IV, VIII, and IX classes, whereas all of the *vma* mutants showed broad divalent cation sensitivity (Supplemental Tables S1 and S2). These results suggested that the majority of the *cls* mutants with related Ca^{2+}–*cls* interaction profiles have defects in a similar function.

Riboflavin deficiency of class VI *cls* mutants results in failure to maintain Ca^{2+} homeostasis

To examine further whether *cls* mutants with related Ca^{2+}–*cls* interaction profiles have defects in a similar function, we focused on the class VI *cls* mutants. Class VI contains *gly1*, *rib4*, and *yel045c*, all of which showed a slow growth phenotype in yeast extract/polypeptone/dextrose (YPD) medium and a severe growth defect in Ca^{2+}-rich medium. *RIB4* and *GLY1* encode lumazine synthase and threonine aldolase, respectively, which play a role in the riboflavin biosynthetic pathway. Lumazine synthase synthesizes a precursor of riboflavin (Monschau *et al.*, 1998), and overproduction of threonine aldolase increases riboflavin content (García-Ramírez *et al.*, 1995). *YEL045c* is a dubious open reading frame in the promoter region of *GLY1*. Because the levels of riboflavin are likely reduced in all mutants, we tested whether the Ca^{2+}-sensitive phenotype of the class VI *cls* mutants was suppressed by riboflavin. We found that the Ca^{2+}-sensitive growth phenotype of *rib4* was completely suppressed by riboflavin, whereas the other class VI mutants were only partially suppressed (Figure 4A), suggesting that riboflavin is required for Ca^{2+} homeostasis.

To identify whether the class VI *cls* mutants are defective in a particular pathway, we examined vacuolar acidification and sphingolipid metabolism in these mutants. In contrast with the V-ATPase mutants, the class VI mutants have intact quinacrine-positive vacuoles (Figure 4B), suggesting that riboflavin is not critical for vacuolar acidification. We examined the ability to synthesize sphingolipids after wild-type and mutant cells were cultured in YPD medium containing [^3H] palmitic acid for 90 min. The lipids were extracted and separated by thin-layer chromatography (TLC). Consistent with a previous report (Uemura *et al.*, 2003), deletion of the *CSG2* gene, which encodes MIPC synthase, resulted in a drastic decrease in the amounts of MIPC and M(IP)$_2$C and an increase in the amount of IPC (Figure 4C). On the other hand, the lipid composition of the class VI *cls* mutants was quite similar to that of wild-type cells, suggesting that riboflavin is not important for MIPC synthase activity (Figure 4C). We then examined whether failure of Ca^{2+} homeostasis results in an energy imbalance, by measuring the amount of $NADP^+$ and NADPH. We found that class VI *cls* mutants have elevated ratios of $NADP^+$/NADPH concentrations (Figure 4D). The ratio of the concentrations of $NADP^+$/NADPH of *cls2/csg2* was similar to that of wild-type cells. Thus, class VI mutants all exhibited a riboflavin deficiency, causing an elevation of $NADP^+$, possibly due to a failure to maintain Ca^{2+} homeostasis.
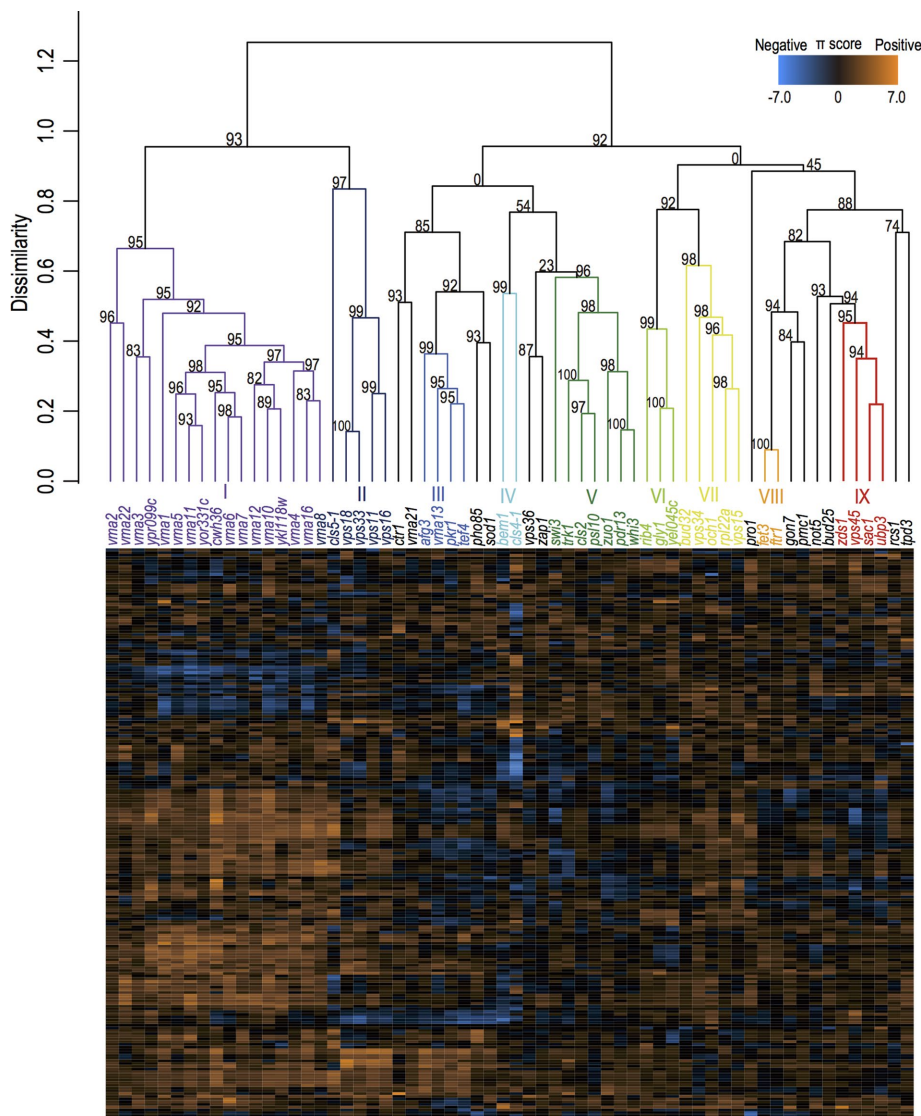
FIGURE 3: Clustering analysis of the *cls* mutants based on similarities of the Ca^{2+}–*cls* interaction profiles. The orange and blue boxes indicate π scores that reflect the degree of positive and negative Ca^{2+}–*cls* interactions. Dissimilarity indicates one minus Pearson product–moment correlation coefficient (PCC) between the vectors of 209 dimensions. The color coding of each class indicates robustly clustered mutant classes at AU *p* > 0.95 calculated by the multiscale bootstrap technique with 3000 iterations (Suzuki and Shimodaira, 2006).

Characterization of Ca^{2+}–*cls* interactions in each functional gene unit

To understand further each class of mutants, we compared positive and negative Ca^{2+}–*cls* interactions in each class (Figure 5A). The 1612 significant interactions (out of 7006 assays; 62 *cls* mutants × 113 parameters) were identified at *p* < 0.05 by Wald test, where the permutation test showed that <387 interactions were expected to be detected by chance (FDR = 0.24). The total number of Ca^{2+}–*cls* interactions was biased, depending on the class. In particular, *cls* mutants of classes I (V-ATPase), II (class C vacuolar protein sorting or C-VPS), and IV (Ca^{2+}-modulated bud formation) showed 9.22, 8.62, and 5.77 times more average interaction density, respectively, than class VIII (Fe ion transporter; Figure 5A, inset). Therefore, the genes of classes I, II, and IV *cls* mutations may be important under conditions of high Ca^{2+}. Note that class I and II *cls* mutations resulted in severe growth defects in Ca^{2+}-rich medium (Supplemental Table S1). Negative interactions were more frequently observed in

particular classes: class III and IV *cls* mutants showed a high proportion of negative Ca^{2+}–*cls* interactions (Figure 5B), on average 8.8 and 7 times higher, respectively, than class I *cls* mutants (Figure 5B, inset). This suggested that each class of mutants has a unique pattern of negative and positive Ca^{2+}–*cls* interactions.

Class IV *cls* mutants shared three significant negative Ca^{2+}–*cls* morphological parameter interactions, which can be attributed to S/G2 and M phases of the cell cycle (Supplemental Figure S3A). Class III *cls* mutants also had three significant negative interactions attributed to G1 and S/G2 phases (Supplemental Figure S3B). Considering that class IV mutations sensitize morphological responses in S/G2 and M phases of the cell cycle and class III mutations sensitize morphological responses in G1 and S/G2 phases, it seemed that sensitized responses during the cell cycle are class specific. This suggested that the morphology-based negative interactions are unique signatures that represent sensitized cellular processes and pathways.

Responses of the Ca^{2+}-sensitive mutants to calcineurin inhibition

Calcineurin is a Ca^{2+}/calmodulin-dependent phosphatase important for several cellular functions, including Ca^{2+} homeostasis (Cyert, 2003). To understand each class of mutants with respect to calcineurin regulation, we systematically investigated the Ca^{2+}-sensitive phenotypes of the *cls* mutants after inactivation of calcineurin. For this purpose, we used the immunosuppressant drug FK506 (Heitman *et al.*, 1991), which specifically inhibits calcineurin activity. Previous studies showed that inactivation of calcineurin confers either alleviating or aggravating effects on cell growth: FK506 suppressed the Ca^{2+}-sensitive growth of *pmc1* (Cunningham and Fink, 1994), whereas it enhanced that of *vma* mutants (Tanida *et al.*, 1995). We found that the Ca^{2+}-sensitive phenotype of 13 *cls* mutants (21%) was suppressed, whereas that of 40 *cls* mutants (65%) was enhanced (Figure 6A, Supplemental Figures S4 and S5, and Supplemental Table S2). Of interest, the *cls* mutants with FK506-enhanced phenotypes accumulated either high or low intracellular Ca^{2+} content (Supplemental Figure S6). Thus, the majority of the *cls* mutants with severely altered Ca^{2+} homeostasis showed FK506-enhanced phenotypes, consistent with previous reports (Tanida *et al.*, 1995; Cunningham and Fink, 1996). Each mutant class had a common response to FK506. Class I, II, and III *cls* mutants showed FK506-enhanced Ca^{2+}-sensitivity, whereas class IV, VI, and VIII mutants showed FK506-suppressed Ca^{2+}-sensitivity (Supplemental Table S1). This suggested that inactivation of calcineurin has similar effects on *cls* mutants with similar functional defects, which supports functional classification of the *CLS* genes based on similarities of the Ca^{2+}–*cls* interaction profile as well.
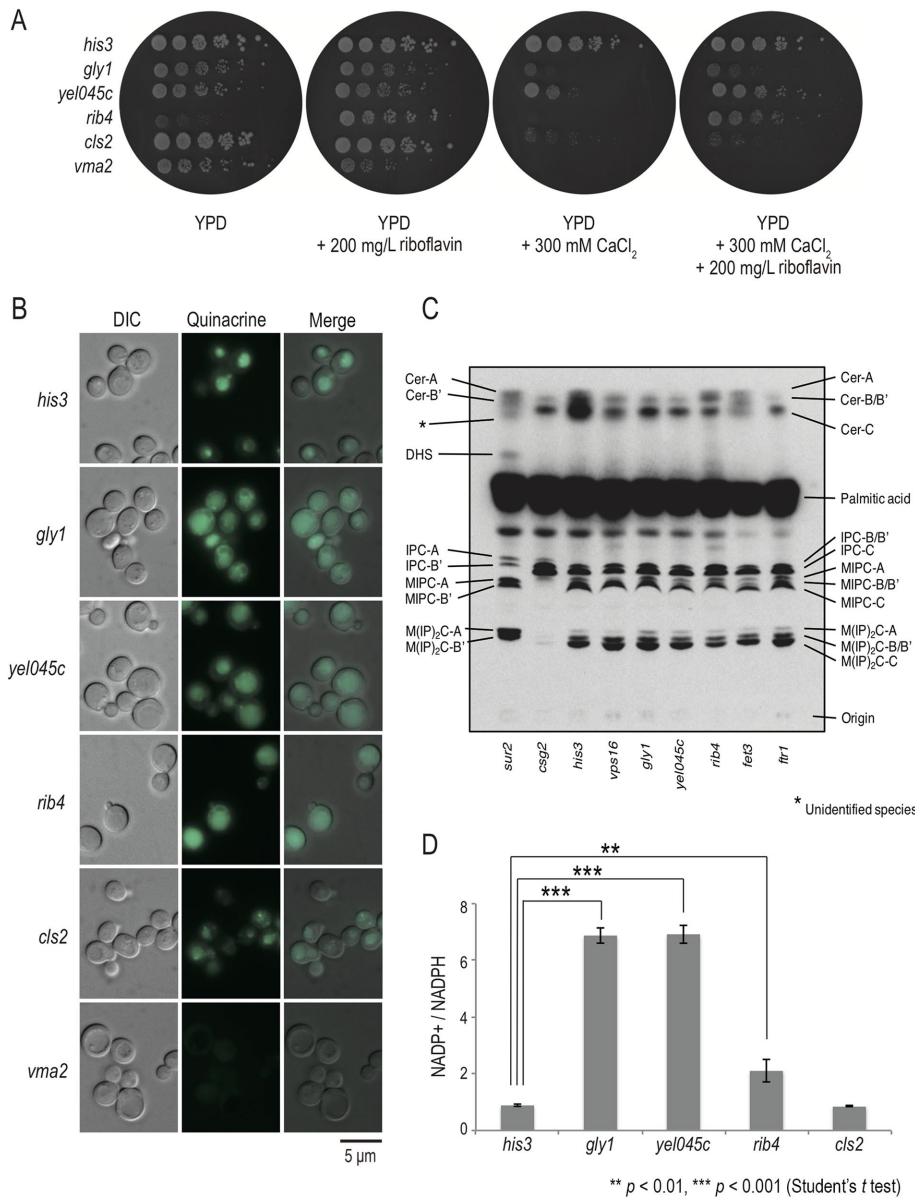
FIGURE 4: Riboflavin deficiency of class VI *cls* mutants induces Ca²⁺ homeostasis. (A) The Ca²⁺-sensitive growth phenotype of the class VI mutants was suppressed by riboflavin. Fivefold serial dilutions of the indicated strains were spotted on YPD, YPD + 200 mg/l riboflavin, YPD + 300 mM CaCl₂, or YPD + 200 mg/l riboflavin + 300 mM CaCl₂ and incubated at 30°C for 4 d. (B) Vacuolar acidification of the class VI mutants. Vacuoles of the indicated strains were stained with quinacrine and examined by fluorescence microscopy. Bar, 5 μm. (C) Lipid composition of the class VI *cls* mutants. Asterisk indicates undefined species. (D) Cellular NADP⁺ measurement of the class VI mutants. NADP⁺ and NADPH were extracted from cells grown in YPD and measured; the ratio of NADP⁺/NADPH is shown as mean ± SD (*n* = 3). Significance levels at **p <0.01 and ***p< 0.001 (Student's *t* test).

Ca²⁺-sensitive phenotypes triggered by inactivation of calcineurin.

Global view of Ca²⁺ homeostasis and Ca²⁺ regulatory pathways

To analyze the similarity of the Ca²⁺–*cls* interaction profiles among the nine classes, we calculated the Pearson product–moment correlation coefficient (PCC) between each pair of the 62 *cls* mutants. We found both positive (red) and negative (blue) correlations between different class mutants (Supplemental Figure S9). Most of the Ca²⁺–*cls* interaction profiles of the class I and II *cls* mutants were negatively correlated with other *cls* mutants, illustrating that class I and II *CLS* genes function in opposite directions from others in Ca²⁺ homeostasis. Note that class I and II mutants shared a common phenotype of FK506-enhanced Ca²⁺ sensitivity. Therefore, calcineurin may function cooperatively with class I and II *CLS* genes to alleviate the deleterious effects of high environmental Ca²⁺. In contrast, most of the Ca²⁺–*cls* interaction profiles of the *cls* mutants in classes IV–IX were positively correlated with one another (Supplemental Figure S9), suggesting that these classes may have similar functional roles in the global Ca²⁺ regulatory network. Class IV, VI, and VIII *cls* mutants all showed FK506-suppressed Ca²⁺ sensitivity. Therefore, calcineurin may function in an opposing manner with classes IV (Ca²⁺-modulated bud formation), VI (riboflavin biosynthesis), and VIII (Fe ion transporter). On the basis of the correlation analysis, we illustrate a global network of Ca²⁺ homeostasis among the *CLS* genes, which act in different cellular compartments and cellular processes (Figure 7). This network provides a systems-level understanding of Ca²⁺ regulatory mechanisms in several organelles. Class I (V-ATPase) and II (C-VPS) proteins, which are localized in the vacuolar membrane and endosome, respectively, and are involved in the maintenance of Ca²⁺ homeostasis, were expected to play central roles in conditions of high Ca²⁺. Multiple interactions are observed in this network of whole-cellular responses to high levels of extracellular Ca²⁺ and are orchestrated by several Ca²⁺ regulatory mechanisms.

FK506-suppressed and -enhanced *cls* mutants discriminated well after the interaction profile PCA. We found that *cls* mutants were distinguishable in two-dimensional Ca²⁺–*cls* interaction space, particularly in the first and second PCs (PC1 and PC2, respectively; Figure 6B and Supplemental Figure S7). FK506-enhanced class I and II mutants are all plotted in the right side with higher PC1 scores and class III with lower PC2 scores. Representative morphological features of PC1 and PC2 are shown in Supplemental Figure S8. Thus, Ca²⁺–*cls* interaction profiles can be used to discriminate between suppression and enhancement of the

DISCUSSION

We applied high-dimensional chemical-genetic interaction profiles to gain a systems-level understanding of Ca²⁺ homeostasis in *S. cerevisiae*. Ca²⁺-induced morphological changes in Ca²⁺-sensitive mutants were quantified from 501 points of view and analyzed to obtain interaction profiles between Ca²⁺ and Ca²⁺-sensitive mutations. Interaction profiles were clustered into nine groups linked to cellular processes involved in vacuolar acidification, cell morphogenesis, Ca²⁺-modulated bud formation, riboflavin biogenesis, protein sorting, and Fe ion transportation, as well as unknown processes
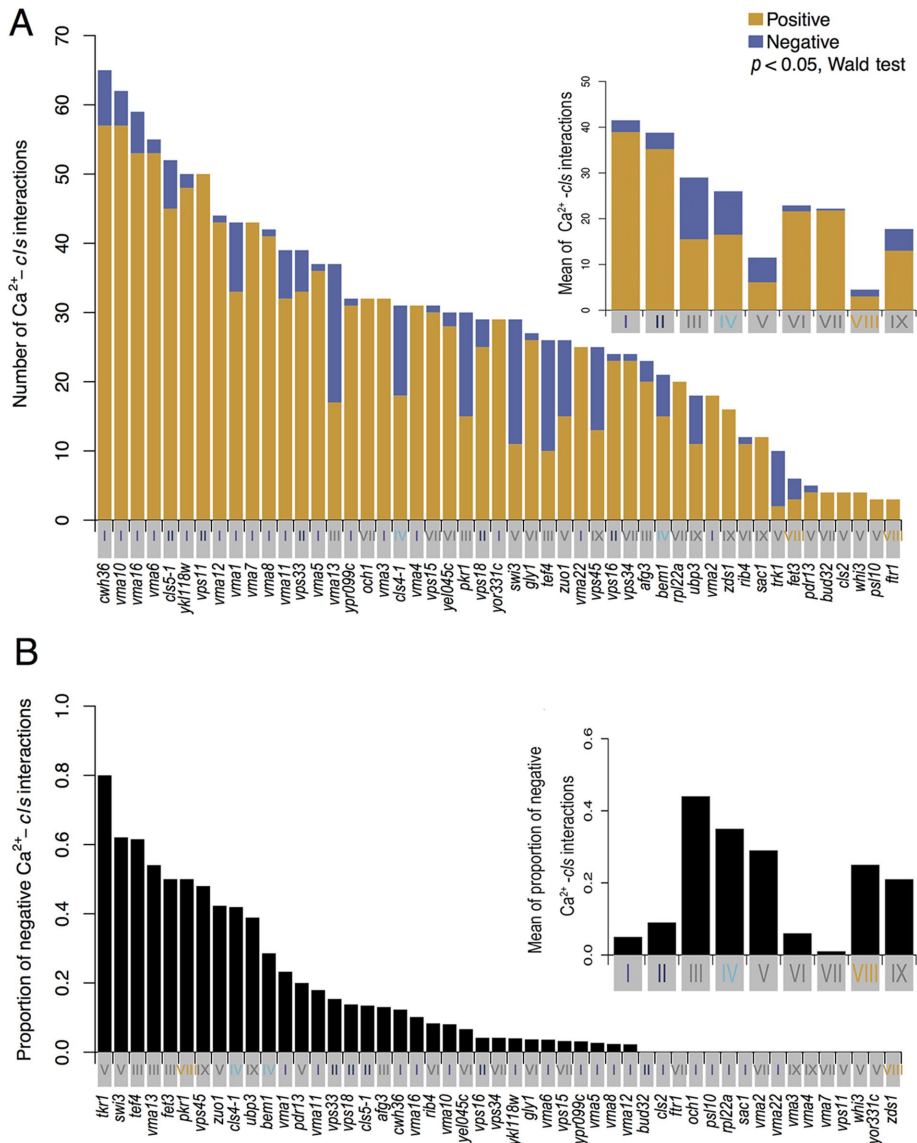
A

Number of Ca²⁺–*cls* interactions

■ Positive
■ Negative
p < 0.05, Wald test

Mean of Ca²⁺–*cls* interactions

cwh36 vma10 vma16 vma6 cls5-1 ykl118w vps11 vma12 vma1 vma7 vma8 vma11 vps33 vma5 vma13 ypr099c och1 vma3 cls4-1 vma4 vps15 yel045c pkr1 vps18 yor331c swi3 gly1 tef4 zuo1 vma22 vps45 vps16 vps34 afg3 bem1 rpl22a vma2 zds1 rib4 sac1 trk1 fet3 pdr13 bud32 cls2 whi3 psl10 ftr1

I II III IV V VI VII VIII IX

B

Proportion of negative Ca²⁺–*cls* interactions

Mean of proportion of negative Ca²⁺–*cls* interactions

tkr1 swi3 tef4 vma13 fet3 pkr1 vps45 zuo1 cls4-1 ubp3 bem1 vma1 pdr13 vma11 vps33 cls5-1 cwh36 vma10 rib4 vma16 yel045c vps34 vps16 ykl118w gly1 vma6 vps15 ypr099c sac1 vma5 vma8 vma12 bud32 cls2 ftr1 psl10 rpl22a sac1 vma2 vma22 vma3 vma4 vma7 vps11 whi3 yor331c zds1

V VII III II VIII V VII IX IV I

FIGURE 5: Properties of the Ca²⁺–*cls* interaction profiles in the *cls* mutants. (A) Number of significant positive and negative interactions in 113 parameters among the indicated *cls* mutants. Orange and blue bars indicate significant positive and negative Ca²⁺–*cls* interactions, respectively ($p < 0.05$, Wald test). Roman numerals (I–IX) of each *cls* mutant correspond to the nine detected classes in Figure 3. Colors highlighting the *cls* mutants indicate high (classes I, II, and IV) and low (class VIII) numbers of Ca²⁺–*cls* interactions, respectively. Inset, mean of Ca²⁺–*cls* interactions in each class (Figure 3). (B) Proportion of significant negative Ca²⁺–*cls* interactions. Colors highlighting the *cls* mutants indicate the high proportion of negative Ca²⁺–*cls* interactions (classes III and IV). Inset, mean of proportion of negative Ca²⁺–*cls* interactions in each class (Figure 3).

known as chemical-genetic interactions. In addition, a negative interaction (chemical synthetic lethality) defines as lethal effects of a chemical compound in a given mutant. Ca²⁺-sensitive mutants showed deleterious effects on growth in conditions of high Ca²⁺, exhibiting a negative interaction with Ca²⁺. In this study, high-dimensional morphological data were employed to describe negative and positive interactions between Ca²⁺ and Ca²⁺-sensitive mutations. Whereas fitness Ca²⁺–*cls* interactions were all negative, morphological Ca²⁺–*cls* interactions were positive and negative, although there were more positive interactions. A negative interaction is interpreted as a Ca²⁺ response sensitized by the *cls* mutation, whereas a positive interaction is caused by suppression, masking changes of the *cls* mutation. Thus, Ca²⁺–*cls* interaction profiles based on morphological changes will likely provide unique data sources.

Studies of several model organisms have proposed that many genes have a few genetic interactions, whereas a small number of genes are highly connected to one other and serve as network hubs (Dixon *et al.*, 2009). Consistent with this, this study revealed that a small number of *CLS* genes exhibit a large number of Ca²⁺–*cls* interactions. The number of Ca²⁺–*cls* interactions was strongly biased in the nine functional classes. In particular, classes I (V-ATPase), II (C-VPS), and IV (Ca²⁺-modulated bud formation) exhibited a large number of Ca²⁺–*cls* interactions. Note that the same classes (I, II, and IV) of *cls* mutations resulted in severe growth defects in Ca²⁺-rich medium. Therefore, the *CLS* genes with many Ca²⁺–*cls* interactions have a large effect, serving as hubs that play key roles in cell proliferation and morphogenesis in conditions of high Ca²⁺.

CLS genes with similar Ca²⁺–*cls* interaction patterns share intracellular functions
Genetic interaction profiles have been used to classify genes based on intracellular functions, proposing that genes that belong to a given biological pathway or process tend to share similar genetic interaction profiles (Tong *et al.*, 2004; Schuldiner *et al.*, 2005; Pan *et al.*, 2006; Jonikas *et al.*, 2009; Costanzo *et al.*, 2010, 2016). Using hierarchical clustering based on the Ca²⁺–*cls* interaction scores, we identified nine functional gene units in Ca²⁺ homeostasis and Ca²⁺ regulatory pathways. This indicated that the *CLS* genes with the same cellular function showed a similar pattern of morphological Ca²⁺–*cls* interactions.

Clustering analysis of 59 *CLS* genes was performed previously based on the similarity of Ca²⁺-induced morphological changes (Ohnuki *et al.*, 2007). Fifty-one percent of the *cls* mutants were classified into seven groups, and three groups were functionally

in the cytoplasm, nucleus, and ER. On the basis of the analysis of the Ca²⁺–*cls* interaction profiles, we constructed a systems-level view of Ca²⁺ homeostasis. Because the deletion mutants of all the nonessential genes in the yeast genome were screened for Ca²⁺-sensitive mutants, this study provides a blueprint for a global understanding of the factors required for Ca²⁺ homeostasis because it covers all the genes essential for proliferation in conditions of high Ca²⁺.

Positive and negative Ca²⁺–*cls* interactions based on morphological changes
In analogy with genetic interactions, combinatorial effects of chemical components and genetic variants to generate a phenotype are

A FK506-suppressed Ca²⁺ sensitivity

YPD

YPD
+ 200 mM CaCl₂

YPD
+ 200 mM CaCl₂
+ 0.4 µg/mLFK506

WT
pmc1

FK506-enhanced Ca²⁺ sensitivity

YPD

YPD
+ 25 mM CaCl₂

YPD
+ 25 mM CaCl₂
+ 0.4 µg/mL FK506

WT
vps16

B

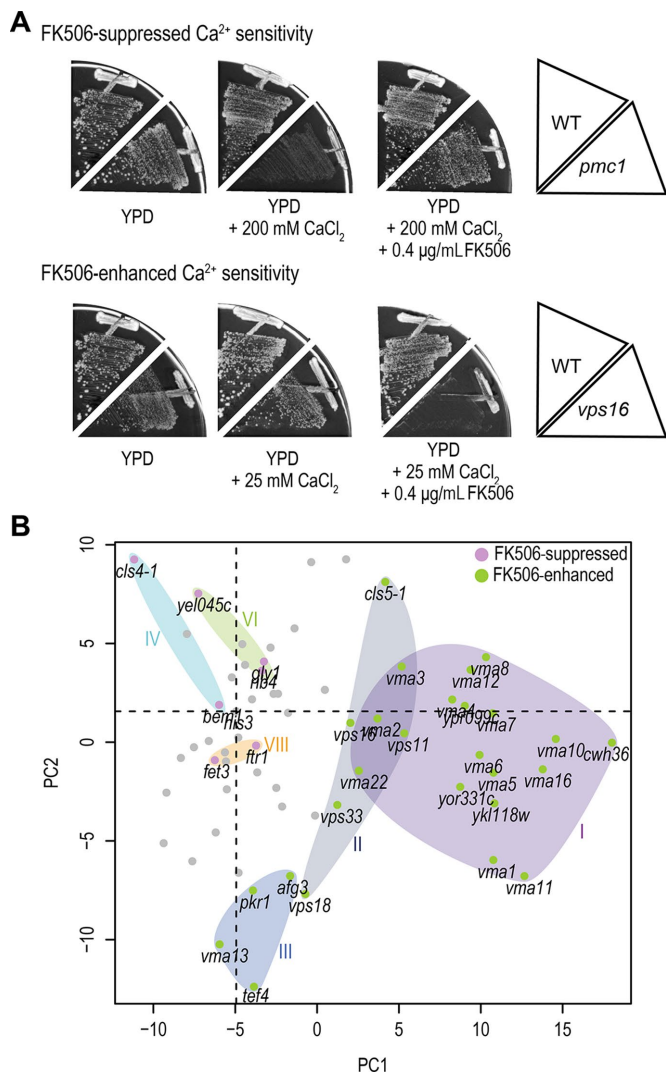**FIGURE 6:** Effects of FK506 on the growth of *cls* mutants in the presence of high Ca²⁺. (A) Example of the aggravating and alleviating effects of FK506 on the growth of *cls* mutants in conditions of high Ca²⁺. The growth of *vps16* (25 mM) and *pmc1* (200 mM) mutants in YPD medium with FK506 (0 and 0.4 µg/ml) in combination with CaCl₂ was tested. Cells were incubated for 4 d at 30°C. Additional conditions tested are shown in Supplemental Figure S4. (B) Scatter plot of PC scores for PC1 and PC2 of the Ca²⁺–*cls* interaction profiles. Strains are represented by their coordinates along the first two PCs. Roman numerals correspond to the detected classes in Figure 3. Purple and green circles indicate FK506-suppressed and -enhanced Ca²⁺ sensitivity, respectively. The *cls* mutants of classes I–III showed FK506-enhanced Ca²⁺ sensitivity, whereas the *cls* mutants of classes IV, VI, and VIII showed FK-506 suppressed Ca²⁺ sensitivity.

annotated. In the present study, we performed an improved clustering analysis based on the Ca²⁺–*cls* interaction profiles, successfully classified 79% of the mutants into nine groups, and functionally annotated six classes. We applied a generalized linear model (GLM) to obtain the Ca²⁺–*cls* interaction profiles from high-dimensional morphological data. After normalization of the traits with the GLM, the interaction terms representing "altered Ca²⁺-response of *cls* mutants" were successfully extracted by calculating the deviation from the expected response values.

The identified clusters can be used to predict the function of the uncharacterized *CLS* genes. One of the examples is class VI, to which three genes, *RIB4*, *GLY1*, and *YEL045C*, were assigned. Rib4p is required for riboflavin biosynthesis, which is a precursor of flavin adenine dinucleotide (FAD; Oltmanns and Bacher, 1972), Gly1p is the glycine biosynthetic enzyme threonine aldolase (McNeil *et al.*, 1994), and *YEL045C* is a dubious open reading frame in the promoter region of the *GLY1* gene. In the filamentous fungus *Ashbya gossypii*, which is closely related to yeast, production of riboflavin was improved by overexpression of the *GLY1* gene (Monschau *et al.*, 1998), suggesting that Gly1p is involved in riboflavin biosynthesis. The Ca²⁺-sensitive growth phenotype of the class VI *cls* mutants was suppressed by the addition of riboflavin. Although the molecular mechanism remains to be elucidated, all class VI *cls* mutants exhibited defects not in vacuolar acidification or sphingolipid biosynthesis, but in perturbation of the energy balance of NADPH.

The class II *cls* mutants, where *cls5-1* was classified with *vps11*, *vps16*, *vps18*, and *vps33*, are known to be core subunits of the CORVET and HOPS complexes, which function in endosome–endosome fusion and homotypic vacuole fusion (Balderhaar and Ungermann, 2013). Although *CLS5* (*PFY1*) encodes profilin, which is required for actin organization, both intracellular Ca²⁺ content and initial Ca²⁺ uptake were elevated in *cls5-1* mutants and four other Ca²⁺-sensitive mutants (Ohya *et al.*, 1986b), suggesting common roles in the maintenance of intracellular Ca²⁺ homeostasis. An immunoprecipitation experiment showed colocalization of Cls5p (Pfy1p) with Vps16p and Vps33p in the vacuolar membrane (Xu and Wickner, 2006). The four *vps* mutants were originally isolated as class I vacuolar morphology (*vam*) mutants, with tiny or invisible vacuoles (Wada *et al.*, 1992), whereas the vacuoles in *cls5-1* mutants were fragmented in the presence of high levels of environmental Ca²⁺ (unpublished data). Therefore, it is likely that Cls5p and the four Vps proteins are involved in vacuolar biogenesis and its functions.

Positive or negative regulation of calcineurin in functional units of Ca²⁺ homeostasis and Ca²⁺ regulatory pathways

We examined how calcineurin is involved in the cellular response to high levels of Ca²⁺ by testing the effect of FK506 on the Ca²⁺ sensitivity of a series of *cls* mutants. Our results suggested that calcineurin functioned either positively or negatively with the functional *CLS* gene units. We confirmed that FK506 enhanced the Ca²⁺ sensitivity of the class I *cls* (*vma*) mutants, which were defective in vacuolar membrane H⁺-ATPase. Several lines of evidence suggest that Ca²⁺ transport into the vacuoles of class I *cls* mutants is decreased (Ohya *et al.*, 1991; Tanida *et al.*, 1995). Yeast cells have compensatory mechanisms for Ca²⁺ transport into the vacuole, such as the Ca²⁺-ATPase Pmc1p (Cunningham and Fink, 1994), and calcineurin positively regulates Pmc1p through activation of the transcription factor Crz1p (Stathopoulos and Cyert, 1997). Because the calcineurin-dependent positive feedback is inhibited in the presence of FK506, Ca²⁺ sequestration into the vacuole is likely decreased in the class I *cls* (*vma*) mutants. Note that *vma3* mutant cells exhibit decreased cytosolic Ca²⁺ and increased organellar Ca²⁺ after treatment with FK506 (Tanida *et al.*, 1995). These findings imply an additional regulatory mechanism in which calcineurin negatively regulates Ca²⁺ sequestration into other organelles such as the ER and the Golgi complex (Cunningham, 2011) under conditions of high Ca²⁺. Previous studies reported that calcineurin may regulate Ca²⁺ sequestration into the ER in cooperation with Cls2p, located in the ER membrane (Beeler *et al.*, 1994; Takita *et al.*, 1995; Tanida *et al.*, 1996). Because FK506 had a minor effect on the Ca²⁺ sensitivity of many of the class V *cls*
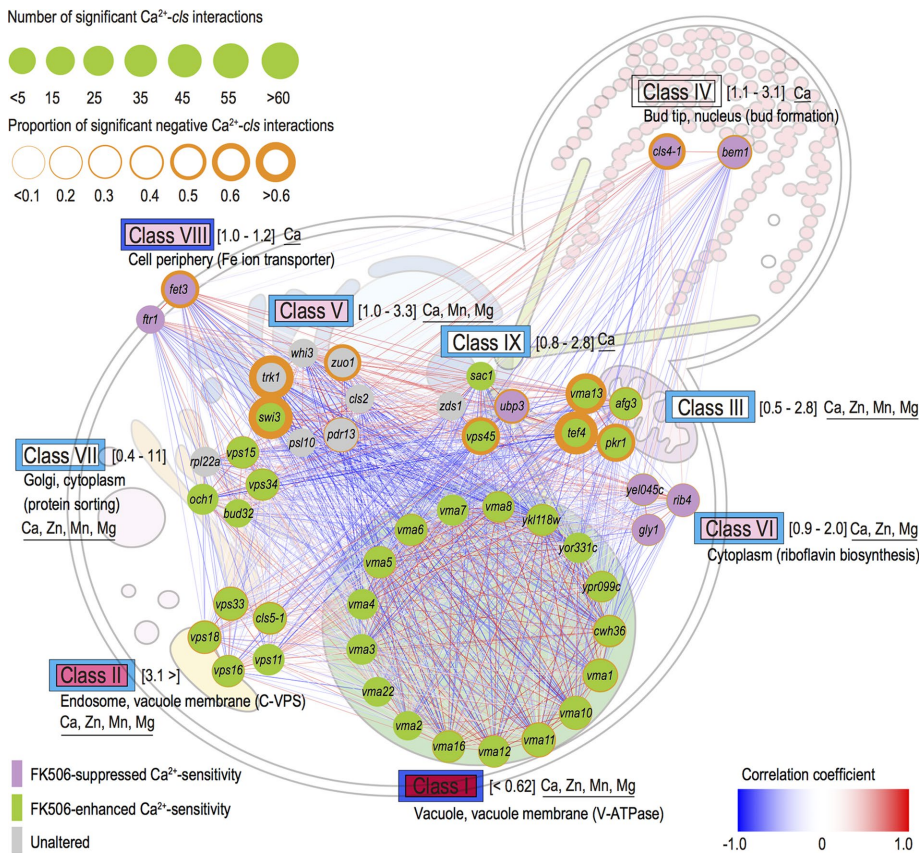
FIGURE 7: Correlation-based network of *cls* mutants. Similarities of Ca²⁺–*cls* interaction profiles were measured for all gene pairs by calculating Pearson product–moment correlation coefficients (PCCs) from the Ca²⁺–*cls* interaction matrix (PCC > 0.2) and are shown as positive (red line) or negative (blue line) correlations of the Ca²⁺–*cls* interaction profile. Node size stands for the average number of significant Ca²⁺–*cls* interactions within each class (*p* < 0.05, Wald test; Figure 5A). In addition, the effects of FK506 on each *cls* mutant are presented as node color (Supplemental Figure S4 and Supplemental Table S2). The node outline indicates the proportion of significant negative Ca²⁺–*cls* interactions of each mutant (Figure 5B). Gene ontologies of each class were obtained from the *Saccharomyces* Genome Database (www.yeastgenome.org/). Relative Ca²⁺ content compared with wild type is shown in brackets. Data from Ohnuki *et al.* (2007) and Yoshida *et al.* (2013). Divalent cation sensitivity is underlined for each class (Supplemental Tables S1 and S2). Whereas all of the *vma* mutants showed broad divalent cation sensitivity, 29 strains showed Ca²⁺-specific sensitivity, such as mutants of IV, VIII, and IX classes (sensitivity to other divalent cation rather than Ca²⁺ decreases the Ca²⁺-specific sensitivity). The inner square next to each class represents quinacrine staining (red, dark pink, light pink, and white illustrate vacuoles that were not stained, vacuoles with morphological defects, stained vacuoles, and a mixture of stained and nonstained vacuoles, respectively). The outer square displays the Pet⁻ phenotype (dark blue, light blue, and white represent minus, mixture of minus and plus, and plus Pet⁻ phenotype, respectively). Data from Ohnuki *et al.* (2007).

elevated cytosolic Ca²⁺ has harmful effects on cellular physiology (Missiaen *et al.*, 2000), one interesting idea is that calcineurin may function as a checkpoint that senses cytosolic Ca²⁺. On elevation of cytosolic Ca²⁺, calcineurin up-regulates Ca²⁺ sequestration to the vacuole and down-regulates bud formation to avoid the toxic effects of Ca²⁺ and maintain Ca²⁺ homeostasis. Note that Ca²⁺ stress results in distinct changes of the global gene expression pattern in yeast through the calcineurin/Crz1p signaling pathway (Yoshimoto *et al.*, 2002). Therefore, in order to test this hypothesis, decipherment of the global gene expression in each *cls* mutant can be considered as a future direction.

Study of the morphological chemical-genetic interaction profiles

In the eukaryotic model organism *S. cerevisiae*, the nonessential gene deletion set (Winzeler *et al.*, 1999) and recently developed libraries of essential genes harboring conditional and hypomorphic alleles (Mnaimneh *et al.*, 2004; Ben-Aroya *et al.*, 2008; Jin *et al.*, 2011; Li *et al.*, 2011) have enabled rapid and comprehensive identification of factors that function in cellular processes of interest. However, functional characterization of these genes, which generally requires gene-by-gene follow-up investigation, remains a bottleneck. Our chemical-genetic interaction approach allows systematic characterization of individual genes, providing a systems-level global view, as well as the molecular bases for cellular processes. Chemical-genetic interaction profiling based on high-dimensional morphological phenotypes described here identifies critical relationships within pathways with multiple inputs (e.g., environmental stress, chemical perturbation, gene perturbation) and outputs (e.g., homeostasis, gene expression, cell cycle progression). We propose that this strategy will be applicable for the systematic analysis of complex cellular processes.

mutants, including *cls2*, class V *CLS* genes may function downstream of calcineurin. Consistent with this, the Ca²⁺–*cls* interaction profiles of class I *cls* (*vma*) mutants negatively correlated with class V *cls* mutants, which are localized to the ER (Ohya *et al.*, 1991; Tanida *et al.*, 1995), suggesting that the opposing calcineurin responses may be a result of the different Ca²⁺–*cls* interaction profiles.

Our results also suggested that calcineurin negatively regulates bud formation under conditions of high Ca²⁺. The Ca²⁺ sensitivity of class IV (Ca²⁺-modulated bud formation) *cls* mutants was suppressed by FK506. The Ca²⁺–*cls* interaction profiles of class IV *cls* mutants tended to negatively correlate with class I *cls* (*vma*) mutants, indicating the opposite response of calcineurin. Because

MATERIALS AND METHODS
Strains and growth conditions
Yeast strains are listed in Supplemental Table S3. All strains are isogenic derivatives of BY4741 (*MAT***a**; *his3*; *leu2*; *met15*; *ura3*; Euroscarf, www.euroscarf.de). Two mutants, *cls4-1* and *cls5-1*, were constructed from YOC138-C (*MAT***a***ade1 cls4-1*; Ohya *et al.*, 1986a) and YOC989 (*MATα leu2 lys2 trp1 ura3 cls5-1*; Yoshida *et al.*, 2013). Briefly, a kanamycin-resistance cassette was amplified from the plasmid pFA6a-GFP(S65T)-kanMX6 (Longtine *et al.*, 1998), targeted to the 3′-untranslated region of the *CLS4* and *CLS5* genes, and located ~250 base pairs downstream of the stop codon. The *cls4-1* and *cls5-1* loci linked to the kanamycin-resistance cassette were amplified by PCR, the amplified fragments were transformed into BY4741, and

Geneticin-resistant transformants were selected. Replacement of the wild-type *CLS4* and *CLS5* genes was confirmed by PCR and sequencing.

S. cerevisiae strains were grown in YPD medium with 1% (wt/vol) Bacto yeast extract (BD Biosciences, San Jose, CA), 2% (wt/vol) polypeptone (Wako Chemicals, Richmond, VA), and 2% (wt/vol) dextrose, pH 5.5. Ca^{2+} sensitivity was tested using 100 mM $CaCl_2$ (Ca^{2+}-rich medium). YPG medium (1% Bacto yeast extract, 2% polypeptone, 2% [vol/vol] glycerol) was applied to survey Pet⁻ phenotypes (inability to grow on a nonfermentable carbon source). Sensitivity to other divalent cations, including 100 mM $MgCl_2$, 3 mM $ZnCl_2$, and 3 mM $MnCl_2$, was also surveyed. Agar (2% [wt/vol]) was used as the solidifier. YPD medium contains 0.4 µg/ml FK506 (Cayman Chemical, Ann Arbor, MI), and various concentrations of $CaCl_2$ (0, 25, 50, 75, and 200 mM) were used to examine the effects of FK506 on cell growth under conditions of high Ca^{2+}. Yeast growth was computationally analyzed via image quantification using ImageJ software, version 1.50i (Abràmoff et al., 2004). One-way analysis of variance (ANOVA) with a negative-binomial probability distribution function was used for statistical analysis. Results were also visually confirmed. To check riboflavin effect on Ca^{2+}-sensitivity, a higher $CaCl_2$ concentration (300 mM; compare with the main experiment, 100 mM) was used to detect any slight effects on suppression of Ca^{2+}-sensitive growth.

Measurements of exchangeable and nonexchangeable Ca^{2+} pools

Intracellular calcium content was measured as described previously (Cunningham and Fink, 1994) with minor modification. Briefly, exponentially growing yeast cells ([1–1.5] × 10⁷ cells/ml) in YPD medium, pH 5.5, were collected, resuspended in YPD medium, pH 5.5, containing ⁴⁵$CaCl_2$ (>10 Ci/g; PerkinElmer, Waltham, MA), and incubated at 30°C for 6.5 h. Protein content was measured using a bicinchoninic acid protein assay kit (Pierce, Rockford, IL) after incubation of each strain in the absence of ⁴⁵$CaCl_2$ in the same conditions as ⁴⁵$CaCl_2$-treated cells. Cultured yeast cells were collected and suspended in 0.2 ml of 10% trichloroacetic acid.

Acquisition and image processing

Ca^{2+} treatment of yeast cells was performed as described previously (Ohnuki et al., 2007). Cells in log phase (8 × 10⁶ cells) in YPD medium were collected, washed once in YPD medium with or without 100 mM $CaCl_2$, and resuspended in 4 ml of the respective medium at a final concentration of 2 × 10⁶ cells/ml. Cells were then incubated for 5 h at 30°C, washed once with YPD medium, fixed in YPD medium supplemented with 3.7% formaldehyde, and resuspended in phosphate-buffered saline (PBS; 0.1 M potassium phosphate buffer, pH 6.5). Triple staining and image analysis using CalMorph (version 1.0) software was performed as previously described (Ohya et al., 2005). CalMorph automatically calculated 501 morphologic parameters of each yeast cell. Cells were stained for three components: fluorescence isothiocyanate–concanavalin A (Sigma-Aldrich, St. Louis, MO), rhodamine–phalloidin (Invitrogen, Carlsbad, CA), and 4′,6-diamidino-2-phenylindole (Sigma-Aldrich), which were used to stain mannoprotein, actin, and the nucleus, respectively. Images of triple-stained cells were captured using an AxioImager M1, a 100× EC-Plan NEO objective lens (Carl Zeiss) equipped with a CoolSNAP HQ cooled charge-coupled device camera (Roper Scientific), and AxioVision software (Carl Zeiss).

Statistical model to assess Ca^{2+}–*cls* interactions

Statistical analyses were performed with R software (www.r-project.org). To statistically assess Ca^{2+}–*cls* interactions for morphological

phenotypes, a GLM, an extension of the normal linear model, was used, which applied not only a Gaussian, but also additional probability distributions (Nelder and Wedderburn, 1972). Models of the probability distributions for the 501 morphological parameters were determined to accommodate the statistical model used in the GLM as previously described (Yang et al., 2014), with some modifications (Yang et al., 2014). Of the 501 parameters calculated by CalMorph, 220 parameters were coefficients of variation (CVs) of their related mean parameters. Estimations of cell-to-cell independent variability were obtained via nonlinear Lowess regression of the CV values as previously described (Yvert et al., 2013) to uncouple concomitant dependence between the CV parameters and the mean parameter values (Levy and Siegal, 2008). After normalization, 220 CV parameters were assumed to be Gaussian-distributed. In addition, 183 parameters, representing the mean cell morphologies with positive continuous values, were assumed to be gamma-distributed, as previously described (Yang et al., 2014). Moreover, 37 parameters, which represented the mean cell morphologies with continuous values ranging from 0 to 1, were assumed as beta- or zero-inflated beta-distributed. The remaining 61 parameters, which represented the ratio of cells in the specimen, were assumed as binomial- or beta-binomial-distributed with or without overdispersion, respectively.

The ANCOVA model, which is a blend of ANOVA and regression in the multiple linear model, was applied for assessment of Ca^{2+} treatment and mutation effects on the cells regarding Gaussian, gamma, beta, zero-inflated beta, binomial, and beta-binomial parameters in the manner of the GLM. The statistical model was defined as follows:

$$\eta\left(y_i\right) = \beta_0 + \beta_1 x_i + \beta_2 d_i + \beta_3 x_1 \cdot d_i + \beta_4 e_i + \varepsilon_i$$

$$d_i = \begin{cases} 0 & \text{did not harbor mutation} \\ 1 & \text{harbored mutation} \end{cases}$$

$$e_i = \begin{cases} 0 & \text{without confounding factor} \\ 1 & \text{with confounding factor} \end{cases}$$

where η is the link function, y_i is a response variable (parameter values), β_0 is the intercept, β_1 is a fixed effect of Ca^{2+} treatment, x_i is a concentration of Ca^{2+} treatment as an explanatory variable for y_i, β_2 is a fixed effect of the *cls* mutation, d_i is an indicator of the mutation as an explanatory variable, β_3 is a fixed effect of the Ca^{2+}–*cls* interaction, of which the explanatory variable $x_i \cdot d_i$ of the interaction term was defined as a product of x_i and d_i in the linear model, β_4 is a fixed effect of the confounding factor, e_i is an indicator of the confounding factor as an explanatory variable, and ε_i is the error. The best model was selected from the combination of probability distributions and the linear models (e.g., zero-inflated beta vs. beta, binomial vs. beta-binomial, with or without cofounding factors) for each parameter based on the Akaike information criterion (AIC; Akaike, 1998). Likelihood ratio test for the interaction term was carried out to detect parameters with significant Ca^{2+}–*cls* interactions among sets of *cls* mutants ($p < 0.05$). The models of probability distributions, corresponding link functions, and descriptions of analyzed parameters are listed in Supplemental Tables S4 and S5, respectively. The Z value, calculated by the Wald test for β_1 of maximum likelihood estimation in each parameter, was used as a degree of Ca^{2+}-induced morphological change of wild-type (*his3Δ* or YPH499) cells in this study (referred to as Z_{wt} in the text and figures).

The Z value, calculated by the Wald test for β_3 of the maximum likelihood estimation in each *cls* mutant, was used as a degree of the Ca^{2+}–*cls* interaction. The π score as a phenotypic interaction score was calculated as follows:

$$\pi = \begin{cases} \beta_3 & \text{if } (\beta_1 < 0 \text{ and } \beta_3 > 0) \text{ or } (\beta_1 < 0 \text{ and } \beta_3 < 0) \\ -\beta_3 & \text{else if } (\beta_1 > 0 \text{ and } \beta_3 < 0) \text{ or } (\beta_1 > 0 \text{ and } \beta_3 > 0) \end{cases}$$

A linear model of dispersion in each parameter was selected from two models by AIC to detect interaction between *cls* mutation and Ca^{2+} treatment in Figure 5, where one of the models was a null model and the other was a linear combination of experimental conditions (each Ca^{2+} concentration in each strain). Of the 501 parameters, 247 were selected to have different dispersion among the experimental conditions by AIC. At $p < 0.05$ by likelihood ratio test, 245 of 501 parameters were detected to have significant interaction(s). Of the 245 parameters, 113 were detected to have significant Ca^{2+} effects on wild type at $p < 0.05$ by Wald test. Among 7006 assays (62 *cls* mutants × 113 parameters), 1612 combinations were detected to have significant interaction at $p < 0.05$ by Wald test as shown in Figure 5, where FDR was estimated as 0.24 by randomization with >2000 iterations.

PCA and hierarchical cluster analysis

To extract the independent morphological features, PCA was performed using morphological data of a null distribution (Ohnuki et al., 2012) with minor modification. The 209 Z values calculated from the parameter values of the 122 replicated wild-type data set (null-distributed data) were subjected to PCA based on the correlation matrix. First, 19 PCs reached 70% of the cumulative contribution ratio (CCR). Significantly correlated parameters with each PC ($p < 0.01$ after Bonferroni correction) were selected and are listed in Supplemental Figure S1.

A similar approach was performed for the identification of independent morphological features correlated with FK506 effects. The independent morphological features were extracted as previously described (Ohnuki et al., 2012). The alleviating and aggravating effects of FK506 on cell growth under conditions of high Ca^{2+} were particularly reflected in the first and second PCs (Supplemental Figure S7B). We found that 67 and 7 parameters were significantly correlated with PC1 and PC2, respectively, at >0.60 of the absolute value of loadings, which is equivalent to the correlation coefficient between the PC score and the π score ($p < 5 \times 10^{-7}$ after Bonferroni correction, Student's t test). In the second PCA, the 67 and the 7 parameter values for PC1 and PC2, respectively, of the 122 replicated wild-type data set (null-distributed data) were used. Parameters with >0.70 of absolute value of the loadings for each PC were selected, and the parameters that correlated with the first five PCs (PC1a–e) and the first three PCs (PC2a–c) are listed in Supplemental Figure S8.

Hierarchical clustering analysis (HCA) for the 62 *cls* mutants was performed as previously described (Ohnuki et al., 2007), with minor modification. Briefly, to exclude correlation among the morphological parameters, PC scores of the Ca^{2+}–*cls* interaction profiles were applied. HCA based on the dissimilarity defined by $1 − R$ (Pearson product–moment correlation coefficient) was applied to the 16 PC scores (80% of the CCR). Clusters were assessed using the R package pvclust tool at AU $p > 0.95$ (Suzuki and Shimodaira, 2006).

Quinacrine staining

For quinacrine labeling, exponentially growing cells were harvested by centrifugation and washed three times with 50 mM sodium phosphate buffer, pH 7.5, containing 2% glucose. Quinacrine was added at a final concentration of 500 µM in 50 mM sodium phosphate buffer, pH 7.5, containing 2% glucose. After a 10-min incubation at 25°C, the cells were collected by centrifugation, washed three times with YPD, pH 7.5, and examined by fluorescence microscopy with a blue filter.

In vivo [3H]palmitic acid labeling

Cells were collected in log phase, resuspended in YPD medium (1.0 A_{600} unit/ml), and labeled with 2.5 µCi of [3H]palmitic acid (American Radiolabeled Chemicals, St. Louis, MO) for 90 min at 30°C. Cells were collected by centrifugation and suspended in extraction buffer (ethanol, water, diethyl ether, pyridine, and 15 N ammonia [15:15:5:1:0.018, vol/vol]). After 15-min incubation at 60°C, extracted lipids were separated from cell debris by 2-min centrifugation at 2000 × g. Lipids in the cell debris were reextracted using extraction buffer. Radioactivity of the lipid solution was measured, and samples of equal radioactivity were used for further analysis. Each lipid solution was alkali treated by incubating with 0.2× volume of 0.5 N NaOH in methanol for 40 min at 37°C and then neutralized with acetic acid. Lipids were dried and suspended in 100 µl of water-saturated butanol. Then 50 µl of water was added, vigorously mixed, and separated into two phases by centrifugation at 9000 × g for 1 min. The butanol phase was collected, and lipids in the water phase were reextracted by adding 100 µl of water-saturated butanol. The two butanol phases were pooled together, dried, and suspended in 20 µl of chloroform/methanol/water (5:4:1 [vol/vol]). Lipids were separated by TLC on Silica Gel 60 high-performance TLC plates (Merck, Whitestation, NJ) with chloroform, methanol, and 4.2 N ammonia (9:7:2 [vol/vol]) as the solvent system.

NADP+ measurement

Cells were grown in YPD to log phase, and each culture of ~108 cells was sampled. Harvested cells were washed with ice-cold PBS and PBS plus 0.01% Triton X-100 and subjected to extraction and detection with Fluoro NADP+/NADPH (Cell Technology, Fremont, CA) according to the manufacturer's instructions, with minor modification. Cells were disrupted with glass beads in lysis buffer and heated at 60°C for 30 min and cooled on ice. Fluorescence was measured at the excitation and emission wavelengths of 540 and 590 nm, respectively, with a Shimadzu RF-5300PC spectrofluorometer.

REFERENCES

Abràmoff MD, Magalhães PJ, Ram SJ (2004). Image processing with ImageJ. Biophotonics Int 11, 36–42.

Akaike H (1998). Information theory and an extension of the maximum likelihood principle. In: Selected Papers of Hirotugu Akaike, New York: Springer, 199–213.

Bachhawat AK, Manolson MF, Murdock DG, Garman JD, Jones EW (1993). The *VPH2* gene encodes a 25 kDa protein required for activity of the yeast vacuolar H+-ATPase. Yeast 9, 175–184.

Balderhaar HJ, Ungermann C (2013). CORVET and HOPS tethering complexes–coordinators of endosome and lysosome fusion. J Cell Sci 126, 1307–1316.

Baryshnikova A, Costanzo M, Myers CL, Andrews B, Boone C (2013). Genetic interaction networks: toward an understanding of heritability. Annu Rev Genomics Hum Genet 14, 111–133.

Beeler T, Gable K, Zhao C, Dunn T (1994). A novel protein, CSG2p, is required for Ca^{2+} regulation in Saccharomyces cerevisiae. J Biol Chem 269, 7279–7284.

Ben-Aroya S, Coombes C, Kwok T, O'Donnell KA, Boeke JD, Hieter P (2008). Toward a comprehensive temperature-sensitive mutant repository of the essential genes of Saccharomyces cerevisiae. Mol Cell 30, 248–258.

Chang Y, Schlenstedt G, Flockerzi V, Beck A (2010). Properties of the intracellular transient receptor potential (TRP) channel in yeast, Yvc1. FEBS Lett 584, 2028–2032.

Costanzo M, Baryshnikova A, Bellay J, Kim Y, Spear ED, Sevier CS, Ding H, Koh JL, Toufighi K, Mostafavi S (2010). The genetic landscape of a cell. Science 327, 425–431.

Costanzo M, VanderSluis B, Koch EN, Baryshnikova A, Pons C, Tan G, Wang W, Usaj M, Hanchard J, Lee SD (2016). A global genetic interaction network maps a wiring diagram of cellular function. Science 353, aaf1420.

Cui J, Kaandorp JA (2006). Mathematical modeling of calcium homeostasis in yeast cells. Cell Calcium 39, 337–348.

Cui J, Kaandorp JA, Ositelu OO, Beaudry V, Knight A, Nanfack YF, Cunningham KW (2009). Simulating calcium influx and free calcium concentrations in yeast. Cell Calcium 45, 123–132.

Cunningham KW (2011). Acidic calcium stores of Saccharomyces cerevisiae. Cell Calcium 50, 129–138.

Cunningham KW, Fink GR (1994). Calcineurin-dependent growth control in Saccharomyces cerevisiae mutants lacking PMC1, a homolog of plasma membrane Ca^{2+} ATPases. J Cell Biol 124, 351–363.

Cunningham KW, Fink GR (1996). Calcineurin inhibits VCX1-dependent H^+/Ca^{2+} exchange and induces Ca^{2+} ATPases in Saccharomyces cerevisiae. Mol Cell Biol 16, 2226–2237.

Cyert MS (2003). Calcineurin signaling in Saccharomyces cerevisiae: how yeast go crazy in response to stress. Biochem Biophys Res Commun 311, 1143–1150.

Cyert MS, Philpott CC (2013). Regulation of cation balance in Saccharomyces cerevisiae. Genetics 193, 677–713.

Demaurex N, Frieden M (2003). Measurements of the free luminal ER Ca^{2+} concentration with targeted "cameleon" fluorescent proteins. Cell Calcium 34, 109–119.

Denis V, Cyert MS (2002). Internal Ca^{2+} release in yeast is triggered by hypertonic shock and mediated by a TRP channel homologue. J Cell Biol 156, 29–34.

Dixon SJ, Costanzo M, Baryshnikova A, Andrews B, Boone C (2009). Systematic mapping of genetic interaction networks. Annu Rev Gene 43, 601–625.

Dunn T, Gable K, Beeler T (1994). Regulation of cellular Ca^{2+} by yeast vacuoles. J Biol Chem 269, 7273–7278.

Eilam Y (1981). Studies on calcium efflux in the yeast Saccharomyces cerevisiae. Microbios 35, 99–110.

Eilam Y, Lavi H, Grossowicz N (1985). Cytoplasmic Ca^{2+} homeostasis maintained by a vacuolar Ca^{2+} transport system in the yeast Saccharomyces cerevisiae. Microbiology 131, 623–629.

Fischer M, Schnell N, Chattaway J, Davies P, Dixon G, Sanders D (1997). The Saccharomyces cerevisiae CCH1 gene is involved in calcium influx and mating. FEBS Lett 419, 259–262.

Förster C, Kane PM (2000). Cytosolic Ca^{2+} homeostasis is a constitutive function of the V-ATPase in Saccharomyces cerevisiae. J Biol Chem 275, 38245–38253.

García-Ramírez JJ, Santos MA, Revuelta JL (1995). The Saccharomyces cerevisiae RIB4 gene codes for 6, 7-dimethyl-8-ribityllumazine synthase involved in riboflavin biosynthesis molecular characterization of the gene and purification of the encoded protein. J Biol Chem 270, 23801–23807.

Halachmi D, Eilam Y (1993). Calcium homeostasis in yeast cells exposed to high concentrations of calcium. Roles of vacuolar H^+-ATPase and cellular ATP. FEBS Lett 316, 73–78.

Heitman J, Movva NR, Hiestand PC, Hall MN (1991). FK 506-binding protein proline rotamase is a target for the immunosuppressive agent FK 506 in Saccharomyces cerevisiae. Proc Natl Acad Sci USA 88, 1948–1952.

Hirata R, Umemoto N, Ho M, Ohya Y, Stevens T, Anraku Y (1993). VMA12 is essential for assembly of the vacuolar $H(+)$-ATPase subunits onto the vacuolar membrane in Saccharomyces cerevisiae. J Biol Chem 268, 961–967.

Ho MN, Hirata R, Umemoto N, Ohya Y, Takatsuki A, Stevens T, Anraku Y (1993). VMA13 encodes a 54-kDa vacuolar $H(+)$-ATPase subunit required for activity but not assembly of the enzyme complex in Saccharomyces cerevisiae. J Biol Chem 268, 18286–18292.

Iida H, Nakamura H, Ono T, Okumura MS, Anraku Y (1994). MID1, a novel Saccharomyces cerevisiae gene encoding a plasma membrane protein, is required for Ca^{2+} influx and mating. Mol Cell Biol 14, 8259–8271.

Jin K, Li J, Vizeacoumar FS, Li Z, Min R, Zamparo L, Vizeacoumar FJ, Datti A, Andrews B, Boone C (2011). PhenoM: a database of morphological phenotypes caused by mutation of essential genes in Saccharomyces cerevisiae. Nucleic Acids Res D687–D694.

Jonikas MC, Collins SR, Denic V, Oh E, Quan EM, Schmid V, Weibezahn J, Schwappach B, Walter P, Weissman JS (2009). Comprehensive characterization of genes required for protein folding in the endoplasmic reticulum. Science 323, 1693–1697.

Kane PM (2006). The where, when, and how of organelle acidification by the yeast vacuolar H-ATPase. Microbiol Mol Biol Rev 70, 177–191.

Kwok EY, Severance S, Kosman DJ (2006). Evidence for iron channeling in the Fet3p–Ftr1p high-affinity iron uptake complex in the yeast plasma membrane. Biochemistry 45, 6317–6327.

Levy SF, Siegal ML (2008). Network hubs buffer environmental variation in Saccharomyces cerevisiae. PLoS Biol 6, e264.

Li Z, Vizeacoumar FJ, Bahr S, Li J, Warringer J, Vizeacoumar FS, Min R, VanderSluis B, Bellay J, DeVit M (2011). Systematic exploration of essential yeast gene function with temperature-sensitive mutants. Nat Biotechnol 29, 361–367.

Longtine MS, III McKenzie A, Demarini DJ, Shah NG, Wach A, Brachat A, Philippsen P, Pringle JR (1998). Additional modules for versatile and economical PCR-based gene deletion and modification in Saccharomyces cerevisiae. Yeast 14, 953–961.

Mani R, Onge RPS, Hartman JL, Giaever G, Roth FP (2008). Defining genetic interaction. Proc Natl Acad Sci USA 105, 3461–3466.

Martin DC, Kim H, Mackin NA, Maldonado-Báez L, Evangelista CC, Beaudry VG, Dudgeon DD, Naiman DQ, Erdman SE, Cunningham KW (2011). New regulators of a high affinity Ca^{2+} influx system revealed through a genome-wide screen in yeast. J Biol Chem 286, 10744–10754.

McNeil J, McIntosh EM, Taylor B, Zhang F-R, Tang S, Bognar A (1994). Cloning and molecular characterization of three genes, including two genes encoding serine hydroxymethyltransferases, whose inactivation is required to render yeast auxotrophic for glycine. J Biol Chem 269, 9155–9165.

Missiaen L, Robberecht W, Van Den Bosch L, Callewaert G, Parys J, Wuytack F, Raeymaekers L, Nilius B, Eggermont J, De Smedt H (2000). Abnormal intracellular Ca^{2+} homeostasis and disease. Cell Calcium 28, 1–21.

Mnaimneh S, Davierwala AP, Haynes J, Moffat J, Peng W-T, Zhang W, Yang X, Pootoolal J, Chua G, Lopez A (2004). Exploration of essential gene functions via titratable promoter alleles. Cell 118, 31–44.

Monschau N, Sahm H, Stahmann K-P (1998). Threonine aldolase overexpression plus threonine supplementation enhanced riboflavin production in Ashbya gossypii. Appl Environ Microbiol 64, 4283–4290.

Nelder J, Wedderburn R (1972). Generalized linear models. J R Stat Soc Ser A 135, 370–384.

Ohnuki S, Kobayashi T, Ogawa H, Kozone I, Ueda J-y, Takagi M, Shin-ya K, Hirata D, Nogami S, Ohya Y (2012). Analysis of the biological activity of a novel 24-membered macrolide JBIR-19 in Saccharomyces cerevisiae by the morphological imaging program CalMorph. FEMS Yeast Res 12, 293–304.

Ohnuki S, Nogami S, Kanai H, Hirata D, Nakatani Y, Morishita S, Ohya Y (2007). Diversity of Ca^{2+}-induced morphology revealed by morphological phenotyping of Ca^{2+}-sensitive mutants of Saccharomyces cerevisiae. Eukaryot Cell 6, 817–830.

Ohtani M, Saka A, Sano F, Ohya Y, Morishita S (2004). Development of image processing program for yeast cell morphology. J Bioinform Comput Biol 1, 695–709.

Ohya Y, Miyamoto S, Ohsumi Y, Anraku Y (1986a). Calcium-sensitive cls4 mutant of Saccharomyces cerevisiae with a defect in bud formation. J Bacteriol 165, 28–33.

Ohya Y, Ohsumi Y, Anraku Y (1986b). Isolation and characterization of Ca^{2+}-sensitive mutants of Saccharomyces cerevisiae. Microbiology 132, 979–988.

Ohya Y, Sese J, Yukawa M, Sano F, Nakatani Y, Saito TL, Saka A, Fukuda T, Ishihara S, Oka S (2005). High-dimensional and large-scale phenotyping of yeast mutants. Proc Natl Acad Sci USA 102, 19015–19020.

Ohya Y, Umemoto N, Tanida I, Ohta A, Iida H, Anraku Y (1991). Calcium-sensitive cls mutants of Saccharomyces cerevisiae showing a Pet-phenotype are ascribable to defects of vacuolar membrane $H(+)$-ATPase activity. J Biol Chem 266, 13971–13977.

Oltmanns O, Bacher A (1972). Biosynthesis of riboflavine in *Saccharomyces cerevisiae*: the role of genes *rib1* and *rib7*. J Bacteriol 110, 818–822.

Pan X, Ye P, Yuan DS, Wang X, Bader JS, Boeke JD (2006). A DNA integrity network in the yeast *Saccharomyces cerevisiae*. Cell 124, 1069–1081.

Pittman JK, Cheng NH, Shigaki T, Kunta M, Hirschi KD (2004). Functional dependence on calcineurin by variants of the *Saccharomyces cerevisiae* vacuolar Ca^{2+}/H^+ exchanger Vcx1p. Mol Microbiol 54, 1104–1116.

Pozos TC, Sekler I, Cyert MS (1996). The product of HUM1, a novel yeast gene, is required for vacuolar Ca^{2+}/H^+ exchange and is related to mammalian Na^+/Ca^{2+} exchangers. Mol Cell Biol 16, 3730–3741.

Sambade M, Alba M, Smardon AM, West RW, Kane PM (2005). A genomic screen for yeast vacuolar membrane ATPase mutants. Genetics 170, 1539–1551.

Schuldiner M, Collins SR, Thompson NJ, Denic V, Bhamidipati A, Punna T, Ihmels J, Andrews B, Boone C, Greenblatt JF (2005). Exploration of the function and organization of the yeast early secretory pathway through an epistatic miniarray profile. Cell 123, 507–519.

Shimodaira H (2002). An approximately unbiased test of phylogenetic tree selection. Syst Biol 51, 492–508.

Stathopoulos AM, Cyert MS (1997). Calcineurin acts through the CRZ1/TCN1-encoded transcription factor to regulate gene expression in yeast. Genes Dev 11, 3432–3444.

Suzuki R, Shimodaira H (2006). Pvclust: an R package for assessing the uncertainty in hierarchical clustering. Bioinformatics 22, 1540–1542.

Takita Y, Ohya Y, Anraku Y (1995). The CLS2 gene encodes a protein with multiple membrane-spanning domains that is important Ca^{2+} tolerance in yeast. Mol Gen Genet 246, 269–281.

Tanida I, Hasegawa A, Iida H, Ohya Y, Anraku Y (1995). Cooperation of calcineurin and vacuolar H^+-ATPase in intracellular Ca^{2+} homeostasis of yeast cells. J Biol Chem 270, 10113–10119.

Tanida I, Takita Y, Hasegawa A, Ohya Y, Anraku Y (1996). Yeast Cls2p/Csg2p localized on the endoplasmic reticulum membrane regulates a non-exchangeable intracellular Ca^{2+} pool cooperatively with calcineurin. FEBS Lett 379, 38–42.

Tong AHY, Lesage G, Bader GD, Ding H, Xu H, Xin X, Young J, Berriz GF, Brost RL, Chang M (2004). Global mapping of the yeast genetic interaction network. Science 303, 808–813.

Uemura S, Kihara A, Inokuchi J-I, Igarashi Y (2003). Csg1p and newly identified Csh1p function in mannosylinositol phosphorylceramide synthesis by interacting with Csg2p. J Biol Chem 278, 45049–45055.

Umemoto N, Ohya Y, Anraku Y (1991). VMA11, a novel gene that encodes a putative proteolipid, is indispensable for expression of yeast vacuolar membrane H(+)-ATPase activity. J Biol Chem 266, 24526–24532.

Wada Y, Ohsumi Y, Anraku Y (1992). Genes for directing vacuolar morphogenesis in *Saccharomyces cerevisiae*. I. Isolation and characterization of two classes of *vam* mutants. J Biol Chem 267, 18665–18670.

Williams RJ (1999). Calcium: the developing role of its chemistry in biological evolution. In: Calcium as a Cellular Regulator, ed. E Carafoli and C Klee, Oxford, UK: Oxford University Press, 3–27.

Winzeler EA, Shoemaker DD, Astromoff A, Liang H, Anderson K, Andre B, Bangham R, Benito R, Boeke JD, Bussey H (1999). Functional characterization of the *S. cerevisiae* genome by gene deletion and parallel analysis. Science 285, 901–906.

Xu H, Wickner W (2006). Bem1p is a positive regulator of the homotypic fusion of yeast vacuoles. J Biol Chem 281, 27158–27166.

Yang M, Ohnuki S, Ohya Y (2014). Unveiling nonessential gene deletions that confer significant morphological phenotypes beyond natural yeast strains. BMC Genomics 15, 932.

Yoshida M, Ohnuki S, Yashiroda Y, Ohya Y (2013). Profilin is required for Ca^{2+} homeostasis and Ca^{2+}-modulated bud formation in yeast. Mol Genet Genomics 288, 317–328.

Yoshimoto H, Saltsman K, Gasch AP, Li HX, Ogawa N, Botstein D, Brown PO, Cyert MS (2002). Genome-wide analysis of gene expression regulated by the calcineurin/Crz1p signaling pathway in Saccharomyces cerevisiae. J Biol Chem 277, 31079–31088.

Yu Y, Jiang YW, Wellinger RJ, Carlson K, Roberts JM, Stillman DJ (1996). Mutations in the homologous ZDS1 and ZDS2 genes affect cell cycle progression. Mol Cell Biol 16, 5254–5263.

Yvert G, Ohnuki S, Nogami S, Imanaga Y, Fehrmann S, Schacherer J, Ohya Y (2013). Single-cell phenomics reveals intra-species variation of phenotypic noise in yeast. BMC Syst Biol 7, 54.

Zhao Y, Du J, Zhao G, Jiang L (2013). Activation of calcineurin is mainly responsible for the calcium sensitivity of gene deletion mutations in the genome of budding yeast. Genomics 101, 49–56.